AGU PUBLICATIONS

Water Resources Research

RESEARCH ARTICLE
10.1002/2016WR018714

Key Points:
- A multiscale multilayer vertically integrated model with vertical dynamics is developed
- It extends the vertically integrated models for layered heterogeneity
- It is much more computationally efficient compared to full 3-D models

Correspondence to:
B. Guo,
boguo@princeton.edu

Citation:
Guo, B., K. W. Bandilla, J. M. Nordbotten, M. A. Celia, E. Keilegavlen, and F. Doster (2016), A multiscale multilayer vertically integrated model with vertical dynamics for CO_2 sequestration in layered geological formations, *Water Resour. Res.*, *52*, 6490–6505, doi:10.1002/2016WR018714.

Received 31 JAN 2016
Accepted 31 JUL 2016
Accepted article online 5 AUG 2016
Published online 25 AUG 2016

A multiscale multilayer vertically integrated model with vertical dynamics for CO_2 sequestration in layered geological formations

Bo Guo[1], Karl W. Bandilla[1], Jan M. Nordbotten[1,2], Michael A. Celia[1], Eirik Keilegavlen[2], and Florian Doster[3]

[1]Department of Civil and Environmental Engineering, Princeton University, Princeton, New Jersey, USA, [2]Department of Mathematics, University of Bergen, Bergen, Norway, [3]Institute of Petroleum Engineering, Heriot-Watt University, Edinburgh, UK

Abstract Efficient computational models are desirable for simulation of large-scale geological CO_2 sequestration. Vertically integrated models, which take advantage of dimension reduction, offer one type of computationally efficient model. The dimension reduction is usually achieved by vertical integration based on the vertical equilibrium (VE) assumption, which assumes that CO_2 and brine segregate rapidly in the vertical due to strong buoyancy and quickly reach pressure equilibrium. However, the validity of the VE assumption requires small time scales of fluid segregation, which may not always be fulfilled, especially for heterogeneous geological formations with low vertical permeability. Recently, Guo et al. (2014a) developed a multiscale vertically integrated model, referred to as the dynamic reconstruction (DR) model, that relaxes the VE assumption by including the vertical two-phase flow dynamics of CO_2 and brine as fine-scale one-dimensional problems in the vertical direction. Although the VE assumption can be relaxed, that model was limited to homogeneous geological formations. Here we extend the dynamic reconstruction model for layered heterogeneous formations, which is of much more practical interest for saline aquifers in sedimentary basins. We develop a new coarse-scale pressure equation to couple the different coarse-scale (vertically integrated) layers, and use the fine-scale dynamic reconstruction algorithm in Guo et al. (2014a) within each individual layer. Together, these form a multiscale multilayer dynamic reconstruction algorithm. Simulation results of the CO_2 plume from the new model are in excellent agreement with full three-dimensional models, with the new algorithm being much more computationally efficient than conventional full three-dimensional models.

1. Introduction

Geological carbon sequestration (GCS) has been proposed and demonstrated as a feasible technology to reduce anthropogenic carbon dioxide (CO_2) emissions into the atmosphere, as part of the framework of global warming mitigation technologies [*Pacala and Socolow*, 2004; *IPCC*, 2005; *Michael et al.*, 2010; *Celia et al.*, 2015]. For GCS to be an effective carbon mitigation strategy, several engineering questions have to be answered related to CO_2 storage capacity, CO_2 injectivity, and containment within the geological storage unit. Depending on the physical processes that are important over the length and time scale associated with specific questions, mathematical models with different levels of complexity can be developed [*Nordbotten and Celia*, 2011; *Bandilla et al.*, 2015; *Celia et al.*, 2015; *Birkholzer et al.*, 2015].

One feature of the GCS system is that the large density difference between CO_2 and the resident brine leads to strong buoyant segregation. If the time scale associated with the fluid segregation is small relative to the time scale associated with the overall simulation time, the two fluid phases may be assumed to always be segregated and to be in pressure equilibrium in the vertical direction. With such a vertical equilibrium (VE) assumption, the general three-dimensional two-phase flow equations can be simplified to a set of two-dimensional equations by vertical integration [e.g., *Bear*, 1972; *Lake*, 1989; *Wu et al.*, 1994; *Gasda et al.*, 2009; *Nordbotten and Celia*, 2011; *Andersen et al.*, 2015; *Nilsen et al.*, 2015], which can even be further simplified to one-dimensional equations by assuming symmetric flows [see, e.g., *Huppert and Woods*, 1995; *Lyle et al.*, 2005; *Nordbotten and Celia*, 2006; *Hesse et al.*, 2008; *MacMinn et al.*, 2010; *Pegler et al.*, 2014; *Zheng et al.*, 2015;

Guo et al., 2016]. The dimension reduction decreases computational effort significantly, which makes the VE models very computationally efficient. However, the applicability of vertically integrated models depends strongly on the vertical equilibrium assumption, which may not always be appropriate, especially for geological formations with relatively low permeability or heterogeneous formations with a wide range of permeabilities, where it takes significant time for the buoyant segregation to occur [*Court et al*., 2012].

Recently, a new type of vertically integrated model that does not rely on the VE assumption has been developed [*Guo et al*., 2014a]. This new model casts the governing equations into two scales: a set of vertically integrated equations in the horizontal domain (coarse scale) and a set of one-dimensional equations resolved in the vertical domain defined over the thickness of the formation (fine scale). Similar to the conventional vertically integrated models, the new model also solves a set of vertically integrated equations (on the coarse scale). However, in contrast to conventional VE models, the new model solves a set of one-dimensional equations in the vertical (fine scale) for the two-phase flow dynamics of CO_2 and brine instead of assuming that the two fluid phases have fully segregated. This new model is referred to as the dynamic reconstruction (DR) model, in the sense that it is a vertically integrated model that dynamically reconstructs the vertical fluid distribution at every time step (as opposed to VE models that use equilibrium fluid distribution). The dynamic reconstruction model maintains the computational advantages of the vertical equilibrium models because the pressure equation is only solved on the coarse scale, and only marginal additional computational effort is required to solve the one-dimensional problems for the vertical dynamics of CO_2 and brine [*Guo et al*., 2014a]. Being able to capture vertical dynamics of CO_2 and brine while maintaining much of the computational advantages of the VE models, the dynamic reconstruction model provides an intermediate model choice between the VE model and full three-dimensional models.

Although the dynamic reconstruction model in *Guo et al*. [2014a] can capture vertical dynamics of CO_2 and brine, it currently only applies to a single homogeneous formation. Here we extend this model to include spatial heterogeneity in the vertical dimension. Specifically, we focus on layered heterogeneity, which is a typical type of heterogeneity for saline aquifers due to their geological deposition history. The geological formation with layered heterogeneity has multiple layers, each of which may have different geological properties, while each of these layers is homogeneous. Such layered systems are common geological structures in the sedimentary aquifers [*Nicot*, 2008; *Birkholzer et al*., 2009; *Zhou et al*., 2010; *Cihan et al*., 2011; *Bandilla et al*., 2012; *Doughty and Freifeld*, 2013], which is a major type of target formations for CO_2 sequestration [*IPCC*, 2005; *Nordbotten and Celia*, 2011; *Birkholzer et al*., 2015]. For these layered systems, we need to model CO_2 migration within and through the layers. We use the same algorithm as that was used in *Guo et al*. [2014a] for CO_2 migration within each individual layer, while for CO_2 migration through the layers, we develop a coarse-scale pressure equation that computes the vertical fluxes of CO_2 and brine between the layers. These fluxes are computed by using the vertical coarse-scale pressure gradient and the fine-scale information (fluid mobilities and geological properties) between the centers of the two layers, leading to an effective coarse-scale Darcy type flux equation in the vertical direction. The coupling through the coarse-scale pressure equations, together with the dynamic reconstruction, form a multilayer dynamic reconstruction model which is able to model CO_2 migration in a geological formation with layered heterogeneity.

In structuring this paper, we first present the general governing equations of two-phase flow, after which we present the mathematical formulations of the multilayer dynamic reconstruction model and the associated numerical scheme we use. This is followed by a comparison of the new model to a conventional three-dimensional simulator, based on modeling results for both an idealized two-layer formation and a more realistic multiple-layer formation with parameters based on the Mt Simon formation of the Illinois Basin. Then we discuss advantages and future directions of the new model. We close the paper with several concluding remarks.

2. Mathematical and Numerical Models

For a geological formation with multiple lateral layers, we cast the entire system into two scales (see Figure 1): a (horizontal) coarse scale that corresponds to the geological layers with different geological properties, and a (vertical) fine scale that represents the thickness of each of those layers. On the coarse scale, we integrate the three-dimensional equations within each layer in the vertical and obtain a coarse-scale pressure equation. The coarse-scale pressure is defined as the pressure in the middle of each layer along the vertical

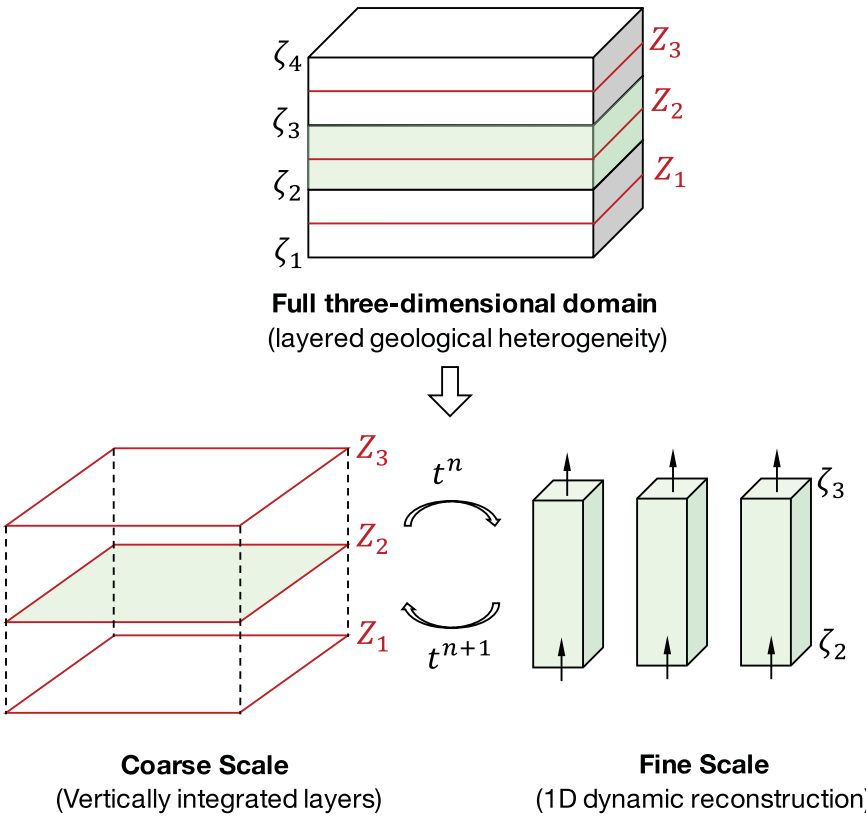

Figure 1. Schematic of the multiscale multilayer dynamic reconstruction algorithm, with three layers as an example. The fine-scale columns belong to the coarse-scale layer, and here we take the columns of the second layer (Z_2) as an example. The arrows in the columns represent the fluxes from layer Z_2 to layer Z_3 and from layer Z_1 to layer Z_2 at the layer boundaries.

direction. To couple all the layers, we develop a multilayer coarse-scale pressure equation that couples the coarse-scale pressure equation at each layer. On the fine scale, we solve the transport equation for the fine-scale saturation and pressure along the vertical columns with the dynamic reconstruction algorithm in *Guo et al*. [2014a]. In the following subsections, we derive the multilayer coarse-scale pressure equation for the coarse-scale layers and briefly review the fine-scale dynamic reconstruction algorithm. Following that, we present the numerical schemes to solve this multiscale framework.

2.1. Full Three-Dimensional Equations

We treat the CO_2 injection system as a two-phase flow problem, neglecting mutual miscibility between the two fluid phases. Note that the multiscale framework in this paper in principle can be extended to include component transport although we have not explored it in detail. We assume immiscibility between the two fluid phases, in part because the mutual solubility between CO_2 and brine is small, up to a few percent [*Nordbotten and Celia*, 2011], and also because this paper focuses on the CO_2 injection period which has a time scale that is short relative to the time scale for convective mixing of CO_2 and brine due to CO_2 dissolution [*Emami-Meybodi et al*., 2015]. Before proceeding to the multiscale algorithms, we first go through the full three-dimensional equations for two-phase flow in porous media as a basis for the development of the multiscale equations.

The general governing equations for two-phase flow in porous media consist of a mass balance equation and an equation of the extended Darcy's law for each of the fluid phases, as shown in equations (1) and (2), respectively

$$\frac{\partial}{\partial t}(\rho_\alpha \phi s_\alpha) + \nabla \cdot (\rho_\alpha \mathbf{u}_\alpha) = \rho_\alpha \psi^\alpha, \tag{1}$$

where $\alpha = b$ or c, representing the fluid phase of brine (b) or CO_2 (c), ρ_α is fluid density, s_α is phase saturation, ϕ is porosity of the geological porous media, $\mathbf{u}_\alpha$ is the volumetric Darcy velocity, and ψ^α is a source term (or sink term if negative).

$$\mathbf{u}_\alpha = -\frac{k_{r,\alpha}\mathbf{k}}{\mu_\alpha}(\nabla p_\alpha - \rho_\alpha \mathbf{g}), \tag{2}$$

where $k_{r,\alpha}$ is relative permeability, $\mathbf{k}$ is the permeability tensor of the geological formation, μ_α is viscosity, p_α is phase pressure, and $\mathbf{g}$ is gravity acceleration. The relative permeability $k_{r,\alpha}$ is commonly parameterized as a function of phase saturation, that is, $k_{r,\alpha}=k_{r,\alpha}(s_\alpha)$. The two phase pressures are related by the capillary pressure, which is also usually taken as an empirical function of phase saturation

$$p_c - p_b = p^{cap}(s_\alpha). \tag{3}$$

Finally, the pore space has to be filled up with the two fluid phases, so the phase saturations should sum to unity

$$s_b + s_c = 1. \tag{4}$$

2.2. Pressure Equation of the Coupled Layers—Coarse Scale

In a multilayer geological formation, the layers are hydraulically connected. Therefore, the coarse-scale individual layer should be coupled with the neighbor layers. That is, the coarse-scale pressure equation will be three-dimensional, where the coarse-scale vertical dimension represents the number of coarse-scale layers. We proceed to derive the coarse-scale pressure equation in two steps. First, we write a vertically integrated mass balance equation for each layer; then we derive an equation for the total fluxes between the layers that couples the coarse-scale pressures of the two layers. The end result is a multilayer pressure equation that couples coarse-scale pressures in the entire formation. Details of the standard procedure of vertical integration for two-phase flow equations can be found in the literature [e.g., *Nordbotten and Dahle*, 2011; *Nordbotten and Celia*, 2011; *Gasda et al*., 2012]. An integration procedure with respect to general pressure profiles (without assuming vertical equilibrium of the fluid phases) can be found in *Guo et al*. [2014a].

Following *Guo et al*. [2014a], the pressure profile in an individual layer can be represented as a reference pressure plus the deviation from the reference pressure, shown in equation (5)

$$p_\alpha(x,y,z,t) = P_\alpha(x,y,t) + \pi_\alpha(x,y,z,t), \tag{5}$$

where $p_\alpha(x,y,z,t)$ is the fine-scale phase pressure at point (x, y, z) and $P_\alpha(x,y,t)$ is the coarse-scale pressure, which we define as the local fine-scale pressure at a reference point in z direction, and $\pi_\alpha(x,y,z,t)$ is the deviation of the fine-scale phase pressure at (x, y, z) from the reference pressure. The definition of the coarse-scale pressure $P_\alpha(x,y,t)$ leads to a coarse-scale capillary pressure P^{cap} defined as the local fine-scale capillary pressure at the reference point. The axis of (x, y) is chosen to be in the plane of the general lateral direction of the formation, and the z axis is the direction orthogonal to the (x, y) axis (assuming upward positive). Note that the reference pressure can be chosen at any point along the z direction. Here we choose the reference pressure to be in the center of the layer (along the z axis).

Integrating equation (1) in the z direction from $z=\zeta_B$ (bottom of the layer) to $z=\zeta_T$ (top of the layer) and summing over the two fluid phases, we obtain [*Guo et al*., 2014a]

$$(c_\phi H + c_b\Phi)S_b\frac{\partial P_b}{\partial t} + (c_\phi H + c_c\Phi)S_c\frac{\partial P_c}{\partial t} + \nabla_\parallel \cdot (\mathbf{U}_b + \mathbf{U}_c) = \Psi^b + \Psi^c - u_{\text{tot},z}|_{\zeta_T} + u_{\text{tot},z}|_{\zeta_B}, \tag{6}$$

where H is the thickness of the geological layer; c_ϕ, c_b, and c_c are the compressibility coefficients (assumed to be constants) of the porous medium, brine, and CO_2, respectively; the "parallel to" subscript $\parallel$ represents the (x, y) plane and $\nabla_\parallel = \frac{\partial}{\partial x}\mathbf{e}_x + \frac{\partial}{\partial y}\mathbf{e}_y$, where $\mathbf{e}_x$ and $\mathbf{e}_y$ are unit vectors in x and y direction; $u_{\text{tot},z}|_{\zeta_T}$ and $u_{\text{tot},z}|_{\zeta_B}$ denote the total fluxes (sum of the CO_2 and brine fluxes) at the top and the bottom of the layer, respectively; the vertically integrated saturations are defined as $S_\alpha = 1/\Phi\int_{\zeta_B}^{\zeta_T}\phi s_\alpha\,dz$ with $\Phi=\int_{\zeta_B}^{\zeta_T}\phi\,dz$; and Ψ^α is the vertically integrated source term of phase α. The vertically integrated horizontal fluxes have the following expressions:

$$\mathbf{U}_\alpha = -\mathbf{K}_\parallel\Lambda_\alpha \cdot (\nabla_\parallel P_\alpha - \rho_\alpha \mathbf{G}) - \int_{\zeta_B}^{\zeta_T}\mathbf{k}_\parallel\lambda_\alpha\nabla_\parallel\pi_\alpha\,dz, \tag{7}$$

where $\mathbf{G}=\mathbf{e}_\parallel\cdot\mathbf{g}+(\mathbf{g}\cdot\mathbf{e}_z)\nabla_\parallel\zeta_B$ and $\mathbf{e}_\parallel=(\mathbf{e}_x,\mathbf{e}_y)^T$; $\mathbf{K}_\parallel=\int_{\zeta_B}^{\zeta_T}\mathbf{k}_\parallel\,dz$; $\lambda_\alpha=\frac{k_{r,\alpha}}{\mu_\alpha}$ is the mobility of fluid phase α; $\Lambda_\alpha = \mathbf{K}_\parallel^{-1}\int_{\zeta_B}^{\zeta_T}\mathbf{k}_\parallel\lambda_\alpha\,dz$ is the vertically integrated mobility of fluid phase α.

The total fluxes at the top ($u_{\mathrm{tot},z}|_{\zeta_T}$) and the bottom ($u_{\mathrm{tot},z}|_{\zeta_B}$) in equation (6) are zero in the single-layer dynamic reconstruction model in *Guo et al.* [2014a]. Thus, equations (6) and (7) give a complete coarse-scale pressure equation for a single-layer system (the functions $\pi_\alpha(x,y,z,t)$ will be computed on the fine scale in section 2.3). However, for a multilayer system, the layers are coupled and $u_{\mathrm{tot},z}|_{\zeta_T}$ and $u_{\mathrm{tot},z}|_{\zeta_B}$ are nonzero. We need to derive a coarse-scale equation for $u_{\mathrm{tot},z}|_{\zeta_T}$ and $u_{\mathrm{tot},z}|_{\zeta_B}$ that couples the neighbor layers. Without loss of generality, we take the flux between layer j and layer $j+1$ as an example (see Figure 2). Note that we choose the coarse-scale brine pressure P_b as the primary variable for pressure ($P_c = P_b + P^{\mathrm{cap}}$). We approximate the total flux between the two layers as

$$u_{\mathrm{tot},j+1/2} = -K_{z,j+1/2}\Lambda_{\mathrm{tot},j+1/2}\left(\frac{P_{b,j+1}-P_{b,j}}{\Delta Z} + \Omega_{1,j+1/2} + \Omega_{2,j+1/2}\right), \tag{8}$$

where $K_{z,j+1/2}$ and $\Lambda_{\mathrm{tot},j+1/2}$ are the effective coarse-scale permeability and total mobility, respectively, between the two layers; $\Omega_{1,j+1/2}$ and $\Omega_{2,j+1/2}$ are terms associated with capillary pressure and gravity, respectively; $\Delta Z = Z_{j+1} - Z_j$ with Z_j and Z_{j+1} the z values of the centers of layer j and $j+1$, respectively; $P_{b,j}$ and $P_{b,j+1}$ are the coarse-scale brine pressures defined as the brine pressure at $Z = Z_j$ and $Z = Z_{j+1}$, respectively.

The coefficients $K_{z,j+1/2}$, $\Lambda_{\mathrm{tot},j+1/2}$, $\Omega_{1,j+1/2}$, and $\Omega_{2,j+1/2}$ are defined based on the fine-scale equations for the two fluid phase fluxes in the vertical direction, which can be written as

$$u_{b,z} = -k_z\lambda_b\left(\frac{\partial p_b}{\partial z} + \rho_b g\right), \tag{9a}$$

$$u_{c,z} = -k_z\lambda_c\left(\frac{\partial p_c}{\partial z} + \rho_c g\right). \tag{9b}$$

Summing equations (9a) and (9b), we obtain the equation for total flux

$$u_{\mathrm{tot},z} = -k_z(\lambda_b+\lambda_c)\frac{\partial p_b}{\partial z} - k_z\lambda_c\frac{\partial p^{cap}}{\partial z} - k_z(\lambda_b\rho_b + \lambda_c\rho_c)g. \tag{10}$$

Rearranging equation (10) gives

$$\frac{\partial p_b}{\partial z} = -\frac{u_{tot,z}}{k(\lambda_b+\lambda_c)} - \frac{\lambda_c}{\lambda_b+\lambda_c}\frac{\partial p^{cap}}{\partial z} - \frac{(\lambda_b\rho_b+\lambda_c\rho_c)}{\lambda_b+\lambda_c}g. \tag{11}$$

Integrating equation (11) from Z_j to Z_{j+1} with respect to z yields

$$\int_{Z_j}^{Z_{j+1}}\frac{\partial p_b}{\partial z}\mathrm{d}z = -\int_{Z_j}^{Z_{j+1}}\frac{u_{\mathrm{tot},z}}{k_z(\lambda_b+\lambda_c)}\mathrm{d}z - \int_{Z_j}^{Z_{j+1}}\frac{\lambda_c}{\lambda_b+\lambda_c}\frac{\partial p^{cap}}{\partial z}\,\mathrm{d}z - \int_{Z_j}^{Z_{j+1}}\frac{(\lambda_b\rho_b+\lambda_c\rho_c)}{\lambda_b+\lambda_c}g\,\mathrm{d}z. \tag{12}$$

The left-side term can be written as

$$\int_{Z_j}^{Z_{j+1}}\frac{\partial p_b}{\partial z}\mathrm{d}z = P_{b,j+1} - P_{b,j}. \tag{13}$$

To derive the coefficients in equation (8), we take $u_{\mathrm{tot},Z_{j+1/2}}$ as an approximation for the average total flux from Z_j to Z_{j+1} in z direction and obtain

$$\int_{Z_j}^{Z_{j+1}}\frac{u_{\mathrm{tot},z}}{k_z(\lambda_b+\lambda_c)}\mathrm{d}z \approx u_{\mathrm{tot},Z_{j+1/2}}\int_{Z_j}^{Z_{j+1}}\frac{1}{k_z(\lambda_b+\lambda_c)}\mathrm{d}z. \tag{14}$$

We note that here we approximate $u_{\mathrm{tot},Z_{j+1/2}}$ as the average total flux from Z_j to Z_{j+1} only to derive the coefficient for equation (8). The actual distribution of total fluxes from Z_j to Z_{j+1} will be computed later in the dynamic reconstruction step as outlined in section 2.3 and presented in detail in Appendix A.

Substituting equations (13) and (14) into equation (12) and after some rearrangement, we obtain

$$u_{\text{tot},Z_{j+1/2}} = -\frac{1}{\frac{1}{\Delta Z}\int_{Z_j}^{Z_{j+1}} \frac{1}{k_z(\lambda_b+\lambda_c)}\,\mathrm{d}z}\left[\frac{P_{b,j+1}-P_{b,j}}{\Delta Z} + \frac{1}{\Delta Z}\int_{Z_j}^{Z_{j+1}} \frac{\lambda_c}{\lambda_b+\lambda_c}\frac{\partial p^{cap}}{\partial z}\,\mathrm{d}z + \frac{1}{\Delta Z}\int_{Z_j}^{Z_{j+1}} \frac{(\lambda_b\rho_b+\lambda_c\rho_c)}{\lambda_b+\lambda_c} g\,\mathrm{d}z\right]. \quad (15)$$

Comparing to equation (8), we obtain

$$K_{z,j+1/2}\Lambda_{\text{tot},j+1/2} = \frac{1}{\frac{1}{\Delta Z}\int_{Z_j}^{Z_{j+1}} \frac{1}{k_z(\lambda_b+\lambda_c)}\,\mathrm{d}z}, \quad (16a)$$

$$\Omega_{1,j+1/2} = \frac{1}{\Delta Z}\int_{Z_j}^{Z_{j+1}} \frac{\lambda_c}{\lambda_b+\lambda_c}\frac{\partial p^{cap}}{\partial z}\,\mathrm{d}z, \quad (16b)$$

$$\Omega_{2,j+1/2} = \frac{1}{\Delta Z}\int_{Z_j}^{Z_{j+1}} \frac{(\lambda_b\rho_b+\lambda_c\rho_c)}{\lambda_b+\lambda_c} g\,\mathrm{d}z. \quad (16c)$$

Note that the derived coarse-scale vertical transmissivity $K_{z,j+1/2}\Lambda_{\text{tot},j+1/2}$ between layer j and $j+1$ is a harmonic average of the fine-scale vertical transmissivities, which is consistent with the classic average scheme of vertical hydraulic conductivities.

Similarly, we can obtain the flux between layer $j-1$ and j, $u_{\text{tot},Z_{j-1/2}}$. Then substituting the two fluxes $u_{\text{tot},Z_{j-1/2}}$ and $u_{\text{tot},Z_{j+1/2}}$ into equation (6), we obtain the coarse-scale pressure equation that couples the neighbor layers $j-1$, j and $j+1$.

$$\begin{aligned}
&(c_\phi H_j + c_b\Phi_j S_{b,j} + c_c\Phi_j S_{c,j})\frac{\partial P_{b,j}}{\partial t} + (c_\phi H_j + c_c\Phi_j)S_{c,j}\frac{\partial P_j^{cap}}{\partial t} \\
&+\nabla_\parallel\cdot\left(-\mathbf{K}_{\parallel,j}(\Lambda_{b,j}+\Lambda_{c,j})\nabla_\parallel P_{b,j} + \mathbf{K}_{\parallel,j}(\rho_b\Lambda_{b,j}+\rho_c\Lambda_{c,j})\mathbf{G}_j - \mathbf{K}_{\parallel,j}\Lambda_{c,j}\nabla P_j^{cap} - \int_{\zeta_j}^{\zeta_{j+1}} \mathbf{k}_\parallel(\lambda_b\nabla_\parallel\pi_b + \lambda_c\nabla_\parallel\pi_c)\,\mathrm{d}z\right) \\
&= K_{z,j+1/2}\Lambda_{\text{tot},j+1/2}\left(\frac{P_{b,j+1}-P_{b,j}}{\Delta Z} + \Omega_{1,j+1/2} + \Omega_{2,j+1/2}\right) \\
&- K_{z,j-1/2}\Lambda_{\text{tot},j-1/2}\left(\frac{P_{b,j}-P_{b,j-1}}{\Delta Z} + \Omega_{1,j-1/2} + \Omega_{2,j-1/2}\right) + \Psi_j^b + \Psi_j^c.
\end{aligned} \quad (17)$$

2.3. Transport in Each Layer—Fine Scale

On the fine scale within each individual layer, we use a dynamic reconstruction algorithm similar to the one developed in *Guo et al.* [2014a]. Here we only outline the main steps of the algorithm, leaving the details of the equations and the algorithm to Appendices A and B.

We need to reconstruct both the saturation and pressure on the fine scale. We reconstruct the fine-scale pressure using a saturation weighted hydrostatic pressure profile with the pressure at the center of the layer (along z axis) fixed as the updated coarse-scale pressure. Other choices for pressure reconstruction have been discussed in *Guo et al.* [2014a, 2014b], and the results to date indicate that the saturation weighted hydrostatic reconstruction gives the best results. The reconstructed fine-scale pressure field is then used to compute the horizontal fine-scale phase fluxes. The total fluxes from the bottom and the top of each layer are computed from equation (8) in the coarse-scale calculation. Then the horizontal fluxes between the columns and the fluxes at the top and bottom of columns are all

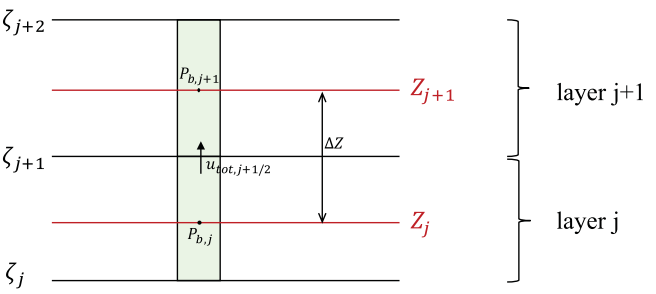

Figure 2. An illustration of the total flux between two layers. Here we take the layers j and $j+1$ as an example. ζ_j, ζ_{j+1}, and ζ_{j+2} are the interlayer boundaries. The light green highlighted areas are two (neighbor) vertical columns of layer j and $j+1$, which have $P_{b,j}$ and $P_{b,j+1}$ as the coarse-scale pressures, respectively. The distance between the centers of the two columns is $\Delta Z = Z_{j+1} - Z_j$. $u_{\text{tot},j+1/2}$ is the total flux from layer j to layer $j+1$, through boundary ζ_{j+1}.

Table 1. Comparisons of MLDR Model and TOUGH2 for a Two-Layer Formation[a]

		t = 1 year				t = 5 years			
		Upper Layer		Lower Layer		Upper Layer		Lower Layer	
Permeability k (mD)	Model	M (%)	R_1 (m)	M (%)	R_2 (m)	M (%)	R_1 (m)	M (%)	R_2 (m)
	MLDR	19.30	45	80.70	575	45.36	210	54.64	1100
$k_{upper}=10,\ k_{lower}=100$	TOUGH2	18.70	60	81.30	550	44.92	220	55.08	1125
	Difference	0.60	15	0.60	25	0.44	10	0.44	25
	MLDR	4.85		95.15	675	14.89	10	85.11	1500
$k_{upper}=1,\ k_{lower}=100$	TOUGH2	4.59		95.41	700	14.98	15	85.02	1550
	Difference	0.26		0.26	25	0.09	5	0.09	50
	MLDR	28.30		71.70	700	59.28	450	40.72	1175
$k_{upper}=10,\ k_{lower}=1000$	TOUGH2	28.71		71.29	725	60.68	450	39.32	1200
	Difference	0.41		0.41	25	1.40	0	1.40	25

[a]M is the mass of CO_2 in each layer normalized by the amount injected, R_1 and R_2 are the extent of the CO_2 plume at the top of layers 1 and 2, respectively, as shown in Figure 3 for example. Blank cells in the column of R1 for the upper layer indicate that CO_2 has not reached the top of the layer.

computed, and we only need to solve the vertical columns (see Figure 1) as independent one-dimensional problems. These one-dimensional problems have "counter-current" type of flow involving buoyancy-driven upward migration of CO_2 and gravity-driven downward drainage of brine, which we solve with a fractional flow formulation as shown in equations (18a) and (18b). See Appendix A for details of the equations. Note that the total fluxes $u_{tot,z}$ are nonzero; they are computed from the fine-scale horizontal total fluxes and the total fluxes at the top and the bottom of the layer. From the fine-scale phase fluxes computed from the fractional flow equations, we then compute and reconstruct the CO_2 saturation in each column.

$$u_{b,z}=f_b\cdot\left(u_{tot,z}-k_z\lambda_c\Delta\rho g+\lambda_c k_z\frac{\partial p^{cap}}{\partial z}\right), \tag{18a}$$

$$u_{c,z}=f_c\cdot\left(u_{tot,z}+k_z\lambda_b\Delta\rho g-\lambda_b k_z\frac{\partial p^{cap}}{\partial z}\right). \tag{18b}$$

2.4. Numerical Scheme and the MLDR Algorithm

The set of multiscale equations in sections 2.2 and 2.3 are solved numerically, including the coarse-scale pressure equation (17) and the fine-scale equations outlined in Appendix A. We use an IMPES (implicit pressure explicit saturation) type method for time stepping and a finite volume method for spatial discretization. The (coarse-scale) pressure is solved implicitly and the (fine-scale) transport is solved explicitly. The two scales are coupled sequentially (see Figure 1). See Appendix B for details of the numerical discretization and the computing procedure for the MLDR algorithm.

3. Model Comparison

The multilayer dynamic reconstruction model (from this point forward, we refer to it as MLDR) developed in this paper can simulate CO_2 migration in a layered heterogeneous formation. To show the capability of the MLDR model, we compare it with the widely used full three-dimensional multiphase flow simulator TOUGH2/ECO2N developed at Lawrence Berkeley National Lab [*Pruess et al.*, 1999; *Pruess*, 2005]. For the comparison, we use two kinds of test cases. The first one has a simple two-layer geological formation with idealized parameter sets, while the other has a four-layer geological formation with parameters from the Mt Simon formation of the Illinois Basin. For the first test case with two layers, we assign different permeabilities to the two layers. Three different scenarios are tested, all of which have a lower permeable layer sitting above a higher permeable layer, but with different permeability contrasts (see Table 1). For the Mt Simon inspired test case, the parameter sets are given in Table 2, and are based on the data from *Zhou et al.* [2010].

Table 2. Geological Parameters of a Four-Layer Formation

Layer #	Thickness (m)	ϕ (-)	k_h (mD)	k_v (mD)
1	7	0.06	4.8	4.8
2	17	0.11	160.3	18.1
3	11	0.08	5.1	5.1
4	25	0.18	891.5	731.5

3.1. A Simple Two-Layer Geological Formation

For the two-layer scenarios, the two layers are both homogeneous and isotropic, and, except

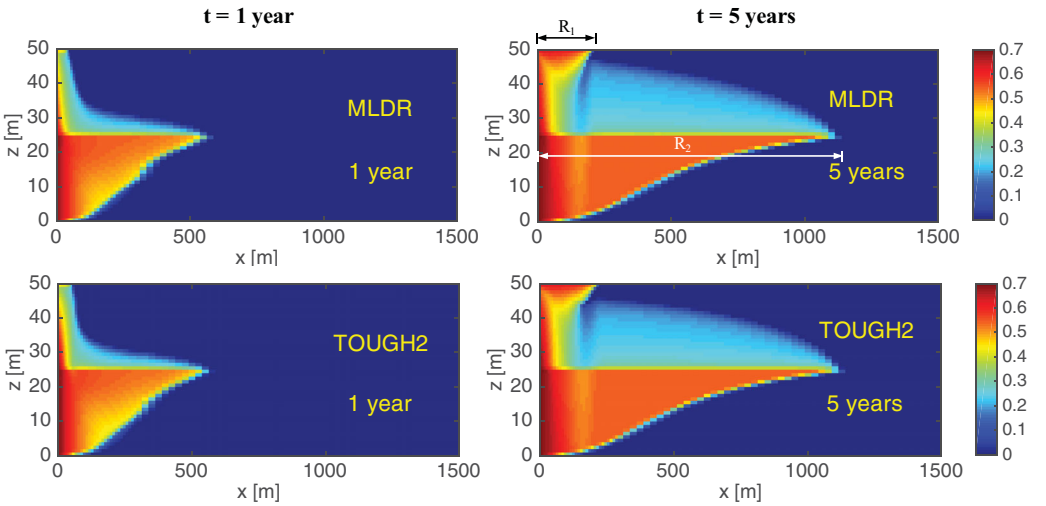

Figure 3. CO_2 plume comparison between the MLDR model and TOUGH2 for a two-layer formation with permeability of 10 and 100 mD in the upper and lower layers, respectively. The first row shows the CO_2 plume from the MLDR model and the second row shows that from TOUGH2. The plumes in the left column are after 1 year of injection and those in the right column are after 5 years of injection. The CO_2 plume extent at the top of each layer is marked in the right top corner panel as an example. Note that the plumes we show here are vertical cross sections of a three-dimensional domain that passes through the injection well, and this applies to Figures 4–6 as well.

for different permeabilities, all other parameters are kept the same for the three scenarios. The pairs of permeabilities for the two layers are (10 mD, 100 mD), (1 mD, 100 mD), and (10 mD, 1000 mD), respectively. Porosity is 0.25 and the system is isothermal with a temperature fixed at 35°C. Density and viscosity of the two fluid phases are fixed as constants in the MLDR model, while TOUGH2 has an equation of state to compute fluid properties from temperature and pressure. For all scenarios, the viscosity and density values used in MLDR for brine are 7.20×10^{-4} Pa s and 1000 kg/m^3. The viscosity and density values used for CO_2 are 7.26×10^{-5} Pa s and 810 kg/m^3 for the first two scenarios (10 mD, 100 mD), (1 mD, 100 mD), and 6.38×10^{-5} Pa s and 756 kg/m^3 for the third scenario (10 mD, 1000 mD). These values were chosen because they correspond most closely to the values used in TOUGH2, thereby allowing for a proper comparison of the numerical solutions. The CO_2 injection rate is 1.0 Mt/year$(=10^9$ kg/year$)$, and CO_2 is injected from a vertical well over the entire thickness of the bottom layer. A boundary condition of hydrostatic pressures is used in the far field of the domain and the formation is initially saturated with brine. Taking advantage of the symmetry of the domain, we choose a quarter domain with an injection rate of 0.25 Mt/year to run the models. We use the van Genuchten model to parameterize relative permeability and capillary pressure, with the characteristic capillary pressure $\alpha^{-1}=10$ Pa and the van Genuchten parameter $m=1-1/n=0.99$ (n is a measure of the pore-size distribution, $n>1$). Note that we have used other sets of van Genuchten parameters, including smaller values of m (e.g., $m=0.41$ adopted from *Zhou et al.* [2010]), and different m values and entry pressures for different layers. The MLDR model can deal with all these parameter sets and produce reasonable results, while the version of TOUGH2 we use runs very slowly for some of the parameter sets. Thus, we only present comparison results for $m=0.99$ and $\alpha^{-1}=10$ Pa. To show that the MLDR can deal with more reasonable parameter sets, we present a set of additional results from MLDR at the end of section 3.1. The residual saturation for brine is $s_{rb}=0.3$ for both layers. Because we only simulate CO_2 injection, the displacements only involve drainage, so CO_2 residual saturations are not relevant. The entire formation has a thickness of 50 m and each layer is 25 m thick. The top of the formation has a depth of 1000 m. The horizontal extent of the quarter domain is 5 km in both x and y directions. The numerical resolution in the vertical is uniform with $\Delta z=1$ m and the grid size in the horizontal progressively increases from $\Delta x=\Delta y=5$ m close to the injection well to $\Delta x=\Delta y=100$ m at the boundary. The number of numerical grid cells is 120 in both x and y directions.

The simulation times for the three scenarios are all 5 years and comparisons are made at 1 and 5 years, respectively. Results from the MLDR model show good agreement with those from TOUGH2 for all the three scenarios, as can be seen in Figures 3–5. We measure the difference with two metrics: the mass of CO_2 in each layer and extent of the CO_2 plume at the top of each layer. As shown in Table 1, the CO_2 mass

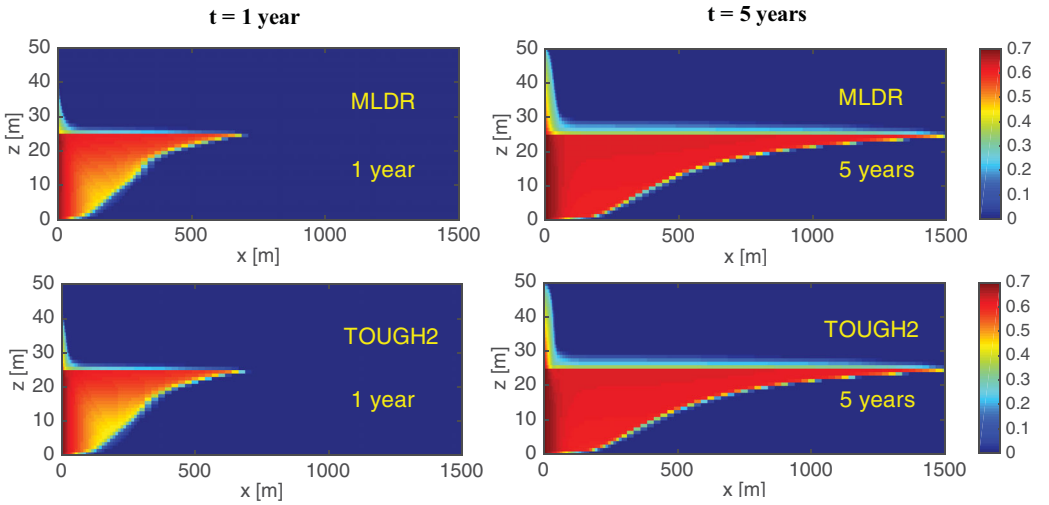

Figure 4. CO_2 plume comparison between the MLDR model and TOUGH2 for a two-layer formation with permeability of 1 and 100 mD in the upper and lower layers, respectively. The first row shows the CO_2 plume from the MLDR model and the second row shows that from TOUGH2. The plumes in the left column are after 1 year of injection and those in the right column are after 5 years of injection.

distribution from the two models in the two layers is very close; the difference between the models is always less than 2% when normalized by the amount injected, with most cases well less than 1%. The extent of the plumes is also in very good agreement. The differences are within one to three numerical grid cells. In terms of computational time, it took 14.6, 12.0, and 63.7 h for the MLDR model to finish the three scenarios, respectively, on a 2011 iMac using a single intel i7 processor. The corresponding computational times are 43, 35, and 78.5 h for TOUGH2 on a cluster with 20 processors. Thus, the MLDR model with our implementation is roughly 20–60 times more efficient than TOUGH2 for the scenarios we considered. We note that MLDR and TOUGH2 are implemented in different programming languages, and TOUGH2 might not scale linearly with the number of processors, nevertheless, the MLDR model is clearly much more computationally efficient than TOUGH2.

Finally, we present one set of additional results from MLDR just to show that MLDR can deal with more reasonable relative permeability and capillary pressure curves. In this test case, all parameters are kept the same as those used in the scenario of (10 mD, 100 mD), except for different relative permeability and capillary pressure curves. We use $m = 0.41$ (adopted from *Zhou et al.* [2010]) for the van Genuchten model, and

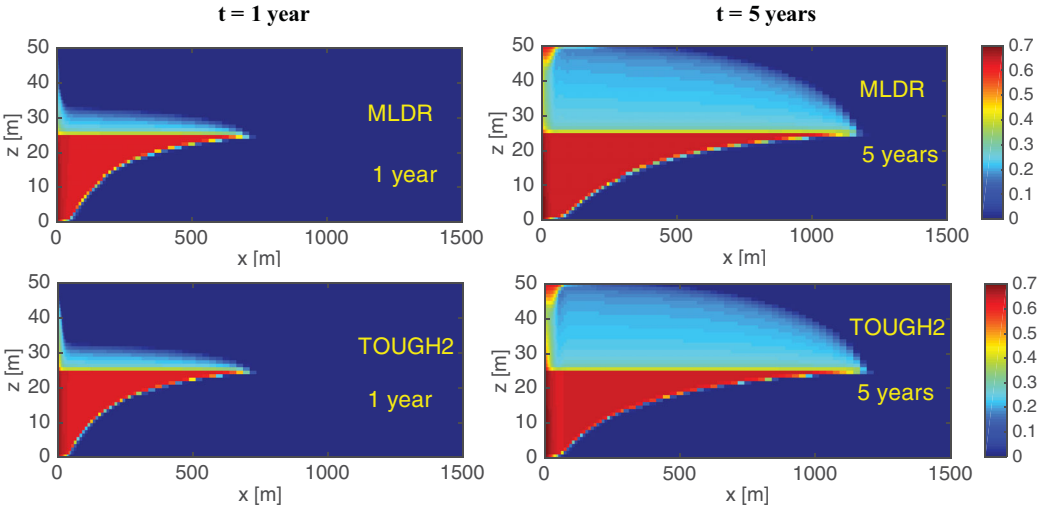

Figure 5. CO_2 plume comparison between the MLDR model and TOUGH2 for a two-layer formation with permeability of 10 and 1000 mD in the upper and lower layers, respectively. The first row shows the CO_2 plume from the MLDR model and the second row shows that from TOUGH2. The plumes in the left column are after 1 year of injection and those in the right column are after 5 years of injection.

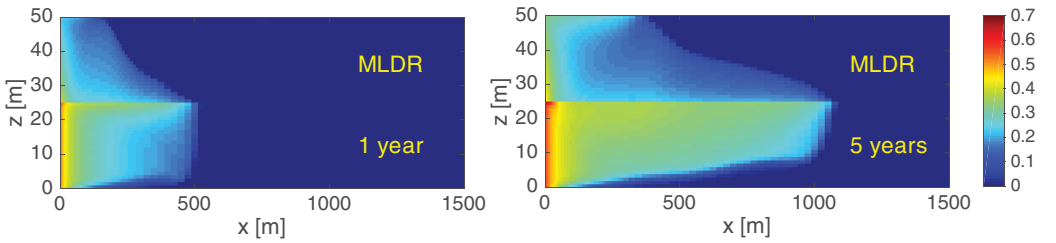

Figure 6. CO_2 plumes from the MLDR model for CO_2 injection into a two-layer geological formation. All parameters are the same as those used in the scenario of (10 mD, 100 mD), except for different relative permeability and capillary pressure curves. $m = 0.41$ is used for the van Genuchten model, and $\alpha^{-1} = 10,000$ Pa is used for the top (low permeability) layer and $\alpha^{-1} = 1000$ Pa is used for the bottom (high permeability) layer. The left and right figures show the results after 1 and 5 years, respectively.

use $\alpha^{-1} = 10,000$ Pa for the top (low permeability) layer and $\alpha^{-1} = 1000$ Pa for the bottom (high permeability) layer. The simulated CO_2 plumes (see Figure 6) are noticeably different from those in Figure 3. This is because the choice of the parameter m ($m = 0.41$) leads to a much wider capillary transition zone and different relative permeabilities compared to the relative permeability curves with $m = 0.99$ used in Figure 3. We have also done test cases with other parameter sets of relative permeability and capillary pressure curves. All of these results are as expected and consistent with our general observations that the MLDR performs well for these kinds of layered systems.

3.2. A Multilayer Geological Formation

To further demonstrate the practical applicability of the MLDR model, we choose a more realistic geological formation with multiple layers. The formation we consider has four layers, and each of them has different geological properties. The geological parameters for the layers (see Table 2) are representative values chosen from the Mt Simon formation of the Illinois Basin as reported in *Zhou et al.* [2010]. We use the same capillary pressure and relative permeability curves, as well as residual saturations for brine and CO_2, as those used in the first test case in section 3.1 for all the four layers. The total thickness of the formation is 60 m and the depth at the top is 2400 m. The size of the domain in the horizontal, the resolution of the numerical grid and the number of grid cells are all kept the same as for the first test case.

Again, the CO_2 plumes from the two models are almost indistinguishable (see Figure 7). We computed the mass of CO_2 and the extent of the CO_2 plume at the top of each individual layer from both simulators. The

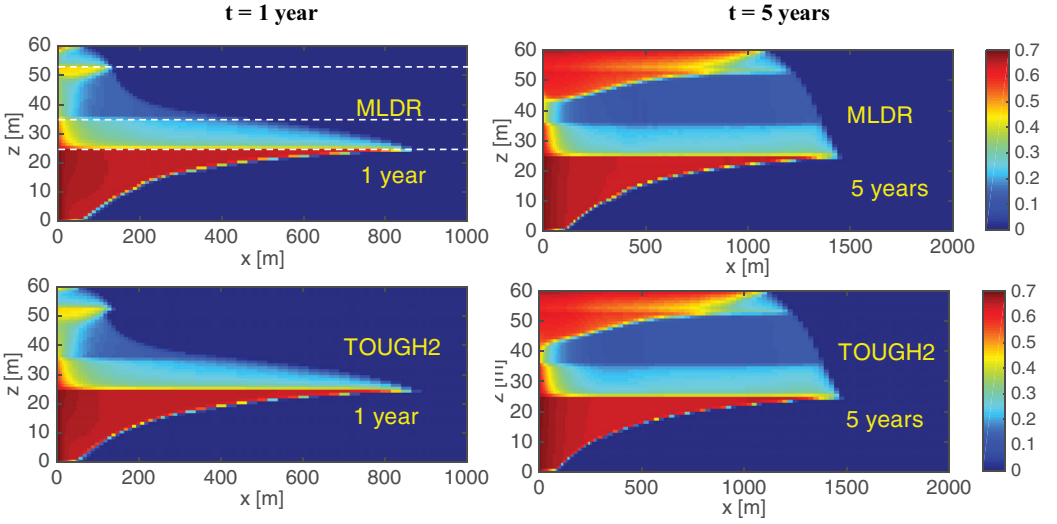

Figure 7. CO_2 plume comparison between the MLDR model and TOUGH2 for a four-layer formation with geological parameters based on Mt Simon formation. The first row shows the CO_2 plume from the MLDR model and the second row shows that from TOUGH2. The plumes in the left column are after 1 year of injection and those in the right column are after 5 years of injection. The layer boundaries between the four layers are marked as white dashed line in the left-top corner panel. From top to bottom, the layers are numbered as 1–4, corresponding that in Table 2.

Table 3. Comparisons of MLDR Model and TOUGH2 for a Four-Layer Formation[a]

		t = 1 year		t = 5 years	
Layer #	Model	M (%)	*R* (m)	M (%)	*R* (m)
	MLDR	0.21	80	10.92	1100
1	TOUGH2	0.22	80	11.05	1125
	Difference	0.01	0	0.13	25
	MLDR	2.75	140	21.83	1225
2	TOUGH2	2.55	140	21.98	1250
	Difference	0.20	0	0.15	25
	MLDR	22.71	450	20.21	1350
3	TOUGH2	23.03	450	20.83	1375
	Difference	0.32	0	0.62	25
	MLDR	74.33	875	47.04	1450
4	TOUGH2	74.20	875	46.13	1475
	Difference	0.13	0	0.91	25

[a]*M* is the mass of CO_2 in each layer normalized by the amount injected, *R* is the extent of the CO_2 plume at the top of each layer.

difference is very small (see Table 3), as is expected from the good visual agreement of the CO_2 plumes in Figure 7. The maximum difference of CO_2 mass is less than 1% of the total mass injected, and the difference of the CO_2 plume extent is all within one grid cell. In terms of computational time, the MLDR simulator used about 50 h on a 2011 iMac using a single intel i7 processor, while it took more than 200 h for TOUGH2 to finish the simulation on a cluster with 10 processors.

Finally, we note that the implementation of the MLDR model assumes constant density and viscosity of the two fluids. The density we used in the simulation shown herein is the saturation weighted density from results of the TOUGH2 simulations, and the viscosity is computed from the pressure corresponding to the computed saturation weighted density. The viscosity and density values used in MLDR for brine are 7.20×10^{-4} Pa s and 1000 kg/m^3, and for CO_2 are 6.33×10^{-5} Pa s and 752 kg/m^3. Despite the assumption of constant density and viscosity in the MLDR model, the predictions of CO_2 plumes are in very good agreement with those from TOUGH2. This is because the density and viscosity do not have much variation in the test cases we considered and therefore it is reasonable to assume constant density and viscosity. In fact, a simple estimation of density and viscosity from the initial pressure in the formation (before CO_2 is injected) is very close to what we got from the TOUGH2 simulation. Nevertheless, for geological formations where variations in density and viscosity are important, an equation of state needs to be implemented for each of the fluid phases in the MLDR model.

4. Discussion

The MLDR model captures the vertical dynamics of CO_2 and brine well both within each individual layer and between the layers. All comparisons of MLDR and TOUGH2 show excellent results. Further, the MLDR algorithm significantly reduces computational effort compared to full three-dimensional models. In the MLDR model, pressures are only solved on the coarse scale. The size of the matrix to solve the pressure equation is significantly reduced compared to a full three-dimensional model, where all the fine-scale pressures needed to be solved. Also, the remaining fine-scale one-dimensional "counter-current" flow problem is easy to solve using the fractional flow formulation. Thus, the multilayer dynamic reconstruction algorithm leads to significant reduction of computational effort. Here we take a geological formation with three layers as an example and give a simple analysis of the complexity of the algorithm. The pressure solver of the MLDR model has a complexity of $O(N_x^2\times N_y^2\times 3^2)$, while the full three-dimensional model has a complexity of $O(N_x^2\times N_y^2\times(N_{z1}+N_{z2}+N_{z3})^2)$. N_x and N_y are the number of grid cells in x and y directions, respectively. N_{z1}, N_{z2}, and N_{z3} are the numbers of vertical grid cells in each of the three layers. This simple analysis shows that the MLDR algorithm reduces the computational cost by an order of $O((N_z/3)^2)$, where $N_z=N_{z1}+N_{z2}+N_{z3}$ is the total number of numerical grids in z direction. It should be noted that the pressure solution is the most computationally intensive part of both the MLDR and conventional three-dimensional algorithms. Although we recognize that TOUGH2 may be slowed partially by the additional computation of component transport and inclusion of compressibility, for the simulations presented here, despite that the implementation of the MLDR is not much optimized, the MLDR model is at least 20 times more computationally efficient compared to TOUGH2; it is 40–60 times faster for most of the simulations we have analyzed. We note that here the comparison of computational efficiency is made by assuming that the processors that MLDR and TOUGH2 use have similar speed and TOUGH2 scales linearly with the number of processors.

The MLDR model uses an explicit scheme for the fine-scale one-dimensional problem; it may require small time steps when the CO_2 and brine segregate rapidly in the vertical. Nevertheless, in the simulations we

have done, the smallest time step does not appear to be unreasonably small, mostly on the order of 0.1 day. Furthermore, when the time step becomes restrictive, several remediation strategies are available. Here we propose three of them. First, we can use larger time steps for the coarse scale than for the fine scale, that is, we compute for several time steps on the fine scale within one coarse-scale time step with a constrain of mass balance. In addition, those fine-scale one-dimensional problems can be computed in parallel because they are independently solved in the MLDR multiscale framework. Finally, if the time step becomes small due to rapid fluid segregation, it is likely that CO_2 and brine reach vertical equilibrium quickly in some of the layers. Thus, it is natural to directly use the (analytical) VE reconstruction without any time step restriction for those layers instead of the dynamic reconstruction algorithm.

For a layered geological formation with significant contrast in permeabilities between the layers, as mentioned in the previous paragraph, VE reconstruction can be used for layers with high permeability where buoyant segregation is fast and the flow is essentially horizontal; while layers with very low permeability may be treated as "aquitard," and we just model the vertical flow, neglecting the horizontal flow, following the tangent law [see, e.g., *Bear*, 1972; *Nordbotten and Celia*, 2011]. Such multilayer systems with alternating "aquifers" and "aquitards" have been studied in groundwater hydrology [e.g., *Hunt*, 1985; *Hemker and Maas*, 1987] and later in the context of CO_2 sequestration for CO_2 migration and leakage through abandoned wells [e.g., *Nordbotten et al*., 2004, 2008; *Cihan et al*., 2011; *Bandilla et al*., 2012]. We note that all of these multilayer models either only focus on single-phase flow or use VE reconstructions for a two-phase flow system. Our MLDR model extends this alternating "aquifer-aquitard" system to a general multilayer model that can include vertical two-phase flow dynamics in layers when VE reconstruction is inappropriate and when flow in low-permeability ("aquitard") formations is not only in the vertical. This extension leads to a new class of hybrid multilayer models where we can design the reconstruction of each layer based on the dominant physics in that layer: use VE or DR reconstructions in the vertical direction depending on the time scales of buoyant segregation of the two fluid phases in aquifers, as well as possible simplified "aquitard" models for the vertical direction when horizontal flow is negligible. For layers with significant heterogeneity with weak horizontal correlation, we can use a full three-dimensional model for that particular layer and still use vertically integrated models with reconstruction algorithms or "aquitard" models for other layers, thereby maintaining computational efficiency. Overall, the MLDR algorithm offers a framework to further develop more advanced hybrid models for CO_2 migration in layered geological formations.

Finally, we point out the similarities and differences for the multiscale multilayer algorithm compared to two existing numerical methods: the Alternating Direction Implicit (ADI) method and the Multiscale Finite Volume Method (MsFVM). The ADI method, developed in the 1950s [*Peaceman and Rachford*, 1955; *Douglas and Rachford*, 1956], is a numerical method that reduces the multidimensional problems into repeated one-dimensional problems with tridiagonal matrices that can be effectively solved using the Thomas algorithm. Subsequent developments of ADI-like methods involved three-dimensional problems solved as a combination of two-dimensional (horizontal) solutions and one-dimensional (vertical) solutions [*Babu and Pinder*, 1984]. This type of alternating direction method is similar to the single-layer DR algorithm [*Guo et al*., 2014a] in that two-dimensional horizontal solutions are coupled with one-dimensional vertical solutions. However, the fundamental difference between the single-layer DR algorithm and the ADI is that the single-layer DR only solves one horizontal plane obtained from vertical integration, as opposed to the ADI method that solves many horizontal planes (with the number equals to the number of vertical grid cells). The MLDR algorithm, an extension to the DR, differs even more from the ADI method. The MLDR coarse scale is a three-dimensional problem—it solves the horizontal flow within each layer and vertical flow between the layers. This kind of two-scale resolution does not exist in the classical ADI methods.

The other numerical method we want to compare is the MsFVM, which is a numerical method that, based on finite-volume discretization, solves the pressure equation on a coarse scale and the transport equation on a fine scale [see, e.g., *Jenny et al*., 2003, 2005]. The MLDR algorithm can be cast into the framework of MsFVM if we think of the coarse-scale cell of the MLDR algorithm as a coarse-scale cell in the MsFVM with $1 \times 1 \times N$ fine-scale cells in x, y, and z directions, respectively. The MsFVM computes coarse-scale effective transmissivities using pressure basis functions, and constructs a coarse-scale system for the pressure equation with the coarse-scale effective transmissivities, then it projects the coarse-scale solutions onto the fine grid by applying the basic functions. The MLDR algorithm, however, only uses the multiscale idea for the vertical dimension. Instead of using specialized basis functions as in MsFVM, the effective transmissivities in

MLDR are derived from vertical integration. Thus, although MLDR can be cast into the general MsFVM framework, it is a noval multiscale algorithm developed by using vertical integration and reconstruction operators.

5. Conclusion

In this paper, we present a multilayer dynamic reconstruction algorithm that can simulate CO_2 migration in deep saline aquifers with layered heterogeneity. The algorithm is based on casting the full three-dimensional governing equations into two scales. The coarse scale is the multiple vertically integrated layers, with coarse-scale pressure only a function of (x,y) in any layer, and a coarse-scale pressure equation that couples all the layers. The fine scale corresponds to the vertical one-dimensional columns defined within the thickness of each layer, on which we solve the two-phase flow dynamics of CO_2 and brine with the dynamic reconstruction algorithm from *Guo et al.* [2014a]. Results show that the MLDR model is in excellent agreement with a full three-dimensional simulator (TOUGH2) for all the test cases we considered. The MLDR model is also much more computationally efficient compared to TOUGH2, with computational time 20–60 times smaller for MLDR.

In summary, the MLDR model is accurate and much more computationally efficient than conventional full three-dimensional simulators, and the computational advantages make it an attractive tool for simulations of CO_2 migration in large-scale CO_2 sequestration systems. In addition, the MLDR model provides a modeling framework for CO_2 migration in geological formation with layered heterogeneities, which can lead to the development of a new class of hybrid models where different reconstructions can be chosen for different layers based on their different time scales of buoyant segregation.

Appendix A: The Fine-Scale Equations

In this appendix section, we outline the fine-scale equations for the transport within each layer. The fine-scale equations are almost identical to those presented in *Guo et al.* [2014a], except that the vertical fluxes at the top and bottom of the layers are nonzero.

On the fine scale, the mass balance equation can be rearranged to focus on the vertical dynamics

$$\frac{\partial(\rho_\alpha \phi s_\alpha)}{\partial t} + \frac{\partial(\rho_\alpha u_{\alpha,z})}{\partial z} = \rho_\alpha \psi_\alpha - \nabla_\parallel \cdot (\rho_\alpha \mathbf{u}_{\alpha,\parallel}). \tag{A1}$$

With the assumption of "slight compressibility" used in *Guo et al.* [2014a], equation (A1) becomes

$$\phi \frac{\partial s_\alpha}{\partial t} + (c_\phi + \phi c_\alpha) s_\alpha \frac{\partial p_\alpha}{\partial t} + \frac{\partial u_{\alpha,3}}{\partial x_3} = \psi^\alpha - \nabla_\parallel \cdot \mathbf{u}_{\alpha,\parallel}, \tag{A2}$$

where the horizontal fluxes can be computed from equation (A3)

$$\mathbf{u}_{\alpha,\parallel} = -\mathbf{k}_\parallel \lambda_\alpha \cdot \left[\nabla_\parallel p_\alpha - \rho_\alpha (\mathbf{e}_\parallel \cdot \mathbf{g})\right]. \tag{A3}$$

Summing equation (A2) over the two fluid phases, we can calculate the total flux, $u_{\mathrm{tot},z}$, in the z direction, from the horizontal fluxes $\mathbf{u}_{\alpha,\parallel}$ and source term ψ_α. Given the total flux values in the z direction, the vertical phase flux $u_{\alpha,z}$ can be computed using the fractional flow form of Darcy's law (equations (18a) and (18b))

$$u_{b,z} = f_b \cdot \left(u_{\mathrm{tot},z} - k_z \lambda_c \Delta\rho g + \lambda_c k_z \frac{\partial p^{cap}}{\partial z}\right), \tag{A4a}$$

$$u_{c,z} = f_c \cdot \left(u_{\mathrm{tot},z} + k_z \lambda_b \Delta\rho g - \lambda_b k_z \frac{\partial p^{cap}}{\partial z}\right), \tag{A4b}$$

where k_z is permeability in z direction, and f_α is the fractional flow function, given by

$$f_\alpha = \frac{\lambda_\alpha}{\lambda_b + \lambda_c}. \tag{A5}$$

Substituting equations (A4a) and (A4b) into equation (A2), we can compute saturations for each fluid phase.

Now given the fine-scale saturations, we can analytically reconstruct the profiles of phase pressures in z direction. We reconstruct the fine-scale pressure using a saturation weighted hydrostatic pressure profile as shown in equations (A6a) and (A6b)

$$\frac{\partial p_c}{\partial z} = -(s_c\rho_c + s_b\rho_b)g + s_b\frac{\partial p^{\mathrm{cap}}(s_b)}{\partial z}, \tag{A6a}$$

$$\frac{\partial p_b}{\partial z} = -(s_c\rho_c + s_b\rho_b)g - s_c\frac{\partial p^{\mathrm{cap}}(s_b)}{\partial z}. \tag{A6b}$$

From equations (A6a) and (A6b), the function π_α in equation (5) can be derived, which gives a fine-scale pressure profile from the coarse-scale pressure. For example, when $\alpha = b$, integration from the bottom of the formation yields

$$p_b(x,y,z,t) = P_b(x,y,t) - \int_{\zeta_B}^{z}\left[(s_c\rho_c + s_b\rho_b)g + s_c\frac{\partial p^{\mathrm{cap}(s_b)}}{\partial z}\right]\mathrm{d}z. \tag{A7}$$

To this point, the fine-scale saturation and pressure profiles are both reconstructed. We can proceed to solve the coarse-scale variables (P_b and P_c) for the next time step. In the following Appendix B, we will outline the numerical scheme to solve the coarse-scale and fine-scale equations, and the step-by-step MLDR algorithm.

Appendix B: Numerical Scheme and the MLDR Algorithm

A time stepping scheme analogous to the implicit pressure-explicit saturation (IMPES) method is used in this paper. We solve pressure on the coarse scale (multiple vertically integrated layers) implicitly, while solve the saturation on the fine scale explicitly. Equation (B1) shows the time discretization of the coarse-scale pressure equation. We linearize the equation by lagging one time step for the coefficients, e.g., mobilities and capillary pressure.

$$\begin{aligned}
&(c_\phi H_j + c_b\Phi_j S^n_{b,j} + c_c\Phi_j S^n_{c,j})\frac{P^{n+1}_{b,j} - P^n_{b,j}}{\Delta t} + (c_\phi H_j + c_c\Phi_j)S^n_{c,j}\frac{P^{cap,n}_j - P^{cap,n-1}_j}{\Delta t} \\
&+\nabla_\parallel\cdot\left(-\mathbf{K}_{\parallel,j}(\Lambda^n_{b,j}+\Lambda^n_{c,j})\nabla_\parallel P^{n+1}_{b,j} + \mathbf{K}_{\parallel,j}(\rho_b\Lambda^n_{b,j} + \rho_c\Lambda^n_{c,j})\mathbf{G}_j - \mathbf{K}_{\parallel,j}\Lambda^n_{c,j}\nabla P^{cap,n}_j - \int_{\zeta_j}^{\zeta_{j+1}}\mathbf{k}_{\parallel,j}(\lambda^n_b\nabla_\parallel\pi^n_b + \lambda^n_c\nabla_\parallel\pi^n_c)\mathrm{d}z\right) \\
&= K_{z,j+1/2}\Lambda^n_{\mathrm{tot},j+1/2}\left(\frac{P^{n+1}_{b,j+1} - P^{n+1}_{b,j}}{\Delta Z} + \Omega^n_{1,j+1/2} + \Omega^n_{2,j+1/2}\right) \\
&- K_{z,j-1/2}\Lambda^n_{\mathrm{tot},j-1/2}\left(\frac{P^{n+1}_{b,j} - P^{n+1}_{b,j-1}}{\Delta Z} + \Omega^n_{1,j-1/2} + \Omega^n_{2,j-1/2}\right) + \Psi^{b,n+1}_j + \Psi^{c,n+1}_j.
\end{aligned} \tag{B1}$$

From equation (B1), we can compute the coarse-scale pressure field. Once we obtain the coarse-scale pressure field, the rest of the numerical solution procedure is similar to the dynamic reconstruction in a single-layer case, and we can directly follow *Guo et al*. [2014a, section 3.3] based on the equations in Appendix A to reconstruct the fine-scale saturation and pressure. A step-by-step computing procedure for the MLDR algorithm is outlined in Table B1.

Table B1. The Computing Procedure for the MLDR Algorithm

Given the initial values of pressure p^0_α and saturation s^0_α:
For all discrete time steps $n = 0, 1, \ldots, N$ **do**
- Compute S^n_α, $P^{\mathrm{cap},n}$, π^n_α, $p^{\mathrm{cap},n}$, λ^n_α, Λ^n_α, $\left(K_{z,j\pm1/2}\Lambda_{\mathrm{tot},j\pm1/2}\right)^n$, $\Omega^n_{1,j\pm1/2}$, $\Omega^n_{2,j\pm1/2}$, and solve for P^{n+1}_b from equation (B1);
- With P^{n+1}_b, compute $u^{n+1}_{\mathrm{tot},Z_{j+1/2}}$ from equation (15);
- Assume $p^{n+1,*}_\alpha = P^{n+1}_\alpha + \pi^n_\alpha$, compute $\mathbf{u}^{n+1,*}_{\alpha,\parallel}$ and $\mathbf{u}^{n+1,*}_{\mathrm{tot},\parallel}$ from equation (A3);
- Compute $u^{n+1,*}_{\mathrm{tot},z}$ by summing equation (A2) over the two fluid phases, and compute $u^{n+1,*}_{\alpha,z}$ from equations (A4a) and (A4b);
- Compute s^{n+1}_α from equation (A2), and analytically reconstruct p^{n+1}_α from equations (A6a) and (A6b).
End for

Acknowledgments
This work was supported in part by the National Science Foundation under grant EAR-0934722; the Department of Energy under grant DE-FE0009563; and the Carbon Mitigation Initiative at Princeton University. We also thank Rainer Helmig from University of Stuttgart for helpful discussions. All of the data used in this study are presented in the paper, including model inputs and outputs.

References

Andersen, O., S. E. Gasda, and H. M. Nilsen (2015), Vertically averaged equations with variable density for CO_2 flow in porous media, *Transp. Porous Media*, *107*(1), 95–127.

Babu, D., and G. Pinder (1984), A finite element-finite difference alternating direction algorithm for three dimensional groundwater transport, in *Finite Elements in Water Resources*, pp. 165–174, Springer, Verlag Berlin Heildelberg.

Bandilla, K. W., M. A. Celia, T. R. Elliot, M. Person, K. M. Ellett, J. A. Rupp, C. Gable, and Y. Zhang (2012), Modeling carbon sequestration in the Illinois basin using a vertically-integrated approach, *Comput. Visualization Sci.*, *15*(1), 39–51.

Bandilla, K. W., M. A. Celia, J. T. Birkholzer, A. Cihan, and E. C. Leister (2015), Multiphase modeling of geologic carbon sequestration in saline aquifers, *Groundwater*, *53*(3), 362–377.

Bear, J. (1972), *Dynamics of Fluids in Porous Media*, Elsevier, N. Y.

Birkholzer, J. T., Q. Zhou, and C.-F. Tsang (2009), Large-scale impact of CO_2 storage in deep saline aquifers: A sensitivity study on pressure response in stratified systems, *Int. J. Greenhouse Gas Control*, *3*(2), 181–194.

Birkholzer, J. T., C. M. Oldenburg, and Q. Zhou (2015), CO_2 migration and pressure evolution in deep saline aquifers, *Int. J. Greenhouse Gas Control*, *40*, 203–220.

Celia, M., S. Bachu, J. Nordbotten, and K. Bandilla (2015), Status of CO_2 storage in deep saline aquifers with emphasis on modeling approaches and practical simulations, *Water Resour. Res.*, *51*, 6846–6892, doi:10.1002/2015WR017609.

Cihan, A., Q. Zhou, and J. T. Birkholzer (2011), Analytical solutions for pressure perturbation and fluid leakage through aquitards and wells in multilayered-aquifer systems, *Water Resour. Res.*, *47*, W10504, doi:10.1029/2011WR010721.

Court, B., K. W. Bandilla, M. A. Celia, A. Janzen, M. Dobossy, and J. M. Nordbotten (2012), Applicability of vertical-equilibrium and sharp-interface assumptions in CO_2 sequestration modeling, *Int. J. Greenhouse Gas Control*, *10*, 134–147.

Doughty, C., and B. M. Freifeld (2013), Modeling CO_2 injection at Cranfield, Mississippi: Investigation of methane and temperature effects, *Greenhouse Gases Sci. Technol.*, *3*(6), 475–490.

Douglas, J., and H. H. Rachford (1956), On the numerical solution of heat conduction problems in two and three space variables, *Trans. Am. Math. Soc.*, *82*, 421–439.

Emami-Meybodi, H., H. Hassanzadeh, C. P. Green, and J. Ennis-King (2015), Convective dissolution of CO_2 in saline aquifers: Progress in modeling and experiments, *Int. J. Greenhouse Gas Control*, *40*, 238–266.

Gasda, S. E., J. M. Nordbotten, and M. A. Celia (2009), Vertical equilibrium with sub-scale analytical methods for geological CO_2 sequestration, *Comput. Geosci.*, *13*(4), 469–481.

Gasda, S. E., H. M. Nilsen, H. K. Dahle, and W. G. Gray (2012), Effective models for CO_2 migration in geological systems with varying topography, *Water Resour. Res.*, *48*, W10546, doi:10.1029/2012WR012264.

Guo, B., K. W. Bandilla, F. Doster, E. Keilegavlen, and M. A. Celia (2014a), A vertically integrated model with vertical dynamics for CO_2 storage, *Water Resour. Res.*, *50*, 6269–6284, doi:10.1002/2013WR015215.

Guo, B., K. W. Bandilla, E. Keilegavlen, F. Doster, and M. A. Celia (2014b), Application of vertically-integrated models with subscale vertical dynamics to field sites for CO_2 sequestration, *Energy Proc.*, *63*, 3523–3531.

Guo, B., Z. Zheng, M. A. Celia, and H. A. Stone (2016), Axisymmetric flows from fluid injection into a confined porous medium, *Phys. Fluids*, *28*(2).

Hemker, C., and C. Maas (1987), Unsteady flow to wells in layered and fissured aquifer systems, *J. Hydrol.*, *90*(3), 231–249.

Hesse, M., F. Orr, and H. Tchelepi (2008), Gravity currents with residual trapping, *J. Fluid Mech.*, *611*, 35–60.

Hunt, B. (1985), Flow to a well in a multiaquifer system, *Water Resour. Res.*, *21*(11), 1637–1641.

Huppert, H. E., and A. W. Woods (1995), Gravity-driven flows in porous layers, *J. Fluid Mech.*, *292*, 55–69.

IPCC. (2005), *IPCC Special Report on Carbon Dioxide Capture and Storage*, edited by B. Metz, et al., Cambridge Univ. Press, N. Y.

Jenny, P., S. Lee, and H. Tchelepi (2003), Multi-scale finite-volume method for elliptic problems in subsurface flow simulation, *J. Comput. Phys.*, *187*(1), 47–67.

Jenny, P., S. Lee, and H. Tchelepi (2005), Adaptive multiscale finite-volume method for multiphase flow and transport in porous media, *Multiscale Model. Simul.*, *3*(1), 50–64.

Lake, L. W. (1989), *Enhanced Oil Recovery*, Prentice Hall, Englewood Cliffs, N. J.

Lyle, S., H. E. Huppert, M. Hallworth, M. Bickle, and A. Chadwick (2005), Axisymmetric gravity currents in a porous medium, *J. Fluid Mech.*, *543*, 293–302.

MacMinn, C. W., M. L. Szulczewski, and R. Juanes (2010), CO_2 migration in saline aquifers. part 1. Capillary trapping under slope and groundwater flow, *J. Fluid Mech.*, *662*, 329–351.

Michael, K., A. Golab, V. Shulakova, J. Ennis-King, G. Allinson, S. Sharma, and T. Aiken (2010), Geological storage of CO_2 in saline aquifers—A review of the experience from existing storage operations, *Int. J. Greenhouse Gas Control*, *4*(4), 659–667.

Nicot, J.-P. (2008), Evaluation of large-scale CO_2 storage on fresh-water sections of aquifers: An example from the Texas gulf coast basin, *Int. J. Greenhouse Gas Control*, *2*(4), 582–593.

Nilsen, H. M., K.-A. Lie, and O. Andersen (2015), Robust simulation of sharp-interface models for fast estimation of CO_2 trapping capacity in large-scale aquifer systems, *Comput. Geosci.*, *20*, 1–21.

Nordbotten, J. M., and M. A. Celia (2006), Similarity solutions for fluid injection into confined aquifers, *J. Fluid Mech.*, *561*, 307–327.

Nordbotten, J. M., and M. A. Celia (2011), *Geological Storage of CO2: Modeling Approaches for Large-Scale Simulation*, John Wiley, Hoboken, N. J.

Nordbotten, J. M., and H. K. Dahle (2011), Impact of the capillary fringe in vertically integrated models for CO_2 storage, *Water Resour. Res.*, *47*, W02537, doi:10.1029/2009WR008958.

Nordbotten, J. M., M. A. Celia, and S. Bachu (2004), Analytical solutions for leakage rates through abandoned wells, *Water Resources Research*, *40*, W04204, doi:10.1029/2003WR002997.

Nordbotten, J. M., D. Kavetski, M. A. Celia, and S. Bachu (2008), Model for CO_2 leakage including multiple geological layers and multiple leaky wells, *Environ. Sci. Technol.*, *43*(3), 743–749.

Pacala, S., and R. Socolow (2004), Stabilization wedges: Solving the climate problem for the next 50 years with current technologies, *Science*, *305*(5686), 968–972.

Peaceman, D. W., and H. H. Rachford Jr. (1955), The numerical solution of parabolic and elliptic differential equations, *J. Soc. Ind. Appl. Math.*, *3*(1), 28–41.

Pegler, S. S., H. E. Huppert, and J. A. Neufeld (2014), Fluid injection into a confined porous layer, *J. Fluid Mech.*, *745*, 592–620.

Pruess, K. (2005), *ECO2N: A TOUGH2 Fluid Property Module for Mixtures of Water, NaCl, and CO2*, Lawrence Berkeley Natl. Lab., Berkeley, Calif.

Pruess, K., C. Oldenburg, and G. Moridis (1999), *TOUGH2 User's Guide Version 2*, Lawrence Berkeley Natl. Lab., Berkeley, Calif.

Wu, Y.-S., P. Huyakorn, and N. Park (1994), A vertical equilibrium model for assessing nonaqueous phase liquid contamination and remediation of groundwater systems, *Water Resour. Res.*, *30*(4), 903–912.

Zheng, Z., B. Guo, I. C. Christov, M. A. Celia, and H. A. Stone (2015), Flow regimes for fluid injection into a confined porous medium, *J. Fluid Mech.*, *767*, 881–909.

Zhou, Q., J. T. Birkholzer, E. Mehnert, Y.-F. Lin, and K. Zhang (2010), Modeling basin-and plume-scale processes of CO_2 storage for full-scale deployment, *Groundwater*, *48*(4), 494–514.